Dual-energy computed tomography of the abdomen: A reliable trouble-shooter

Viswanath Anand Chidambaram[1], Mindy Chu Ming Choong[1] (ID), Chaitra Dhiraj Goud[2] (ID)

[1]Department of Diagnostic Radiology, Singapore General Hospital, [2]Department of Diagnostic Radiology, Woodlands Health, Singapore.

*Corresponding author:
Viswanath Anand Chidambaram,
Department of Diagnostic
Radiology, Singapore General
Hospital, Singapore.

cvananddmrd@gmail.com

ABSTRACT

Dual-energy computed tomography (CT) systems have undergone significant evolution and advancements in technology since they came into clinical practice in 2006. The basic principle of dual-energy is comparing the attenuation of different materials when exposed to high and low energy levels. In this article, we provide a brief overview of the basics of dual-energy CT systems, a pictorial review of commonly encountered abdominal conditions, and its role as a trouble-shooter in various diagnostic difficulties.

Keywords: Dual-energy, Computed tomography, Virtual unenhanced images, Iodine-enhanced images

INTRODUCTION

Routine use of dual-energy computed tomography (CT) in the abdomen can increase diagnostic confidence and lesion detection in oncological imaging for various liver, pancreas, and genitourinary malignancies. Improved detection of non-calcified gallstones, characterization of urinary calculi, differentiation of hyperdense renal cysts from solid renal lesions on single-phase CT by assessment of density on virtual unenhanced images and contrast enhancement on iodine maps, and increased sensitivity in detecting bowel ischemia and inflammation are some of the common instances where dual-energy CT provides ample advantages compared to single-energy CT. In this article, we provide a pictorial review of various abdominal conditions where dual-energy CT can provide valuable information in daily clinical practice.

PRINCIPLES OF DUAL-ENERGY COMPUTED TOMOGRAPHY

Conventional single-energy CT uses the principle of X-ray attenuation to distinguish different materials. It is represented as CT numbers in Hounsfield units (HU), which are calibrated in reference to water. However, CT numbers are erratic and variable due to overlap in material attenuation, thus resulting in a lack of precision to differentiate various materials. On the other hand, dual-energy CT provides material-specific analysis based on the elemental constituents and attenuation differences at different energy levels.[1,2]

The basic principles of X-ray attenuation in any material depend on the photoelectric effect, which causes photon absorption, and the Compton effect, which is responsible for photon scattering. The photoelectric effect is dominant at low energy levels and directly proportional
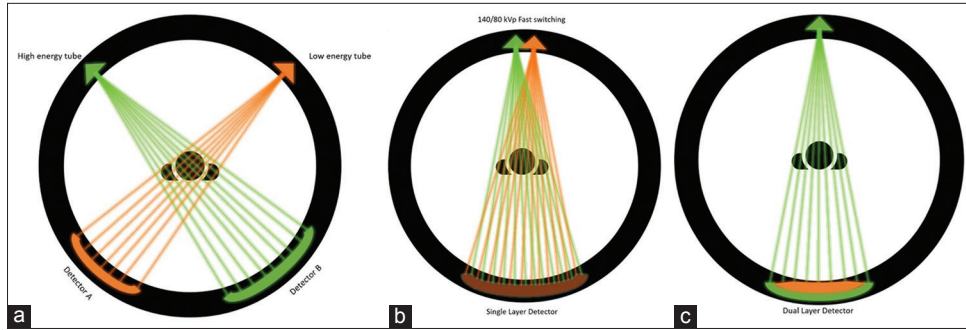
Figure 1: Various dual-energy computed tomography systems (DECT) are currently available on the market. (a) Dual source DECT: two source X-ray tubes are placed orthogonally to each other with corresponding detectors. (b) Rapid voltage switching DECT: single source which is capable of rapid voltage switching between low and high energies with a corresponding single detector. (c) Dual layer DECT: Single source and single detector, which consists of two different layers of detectors to separate low- and high-energy spectra.
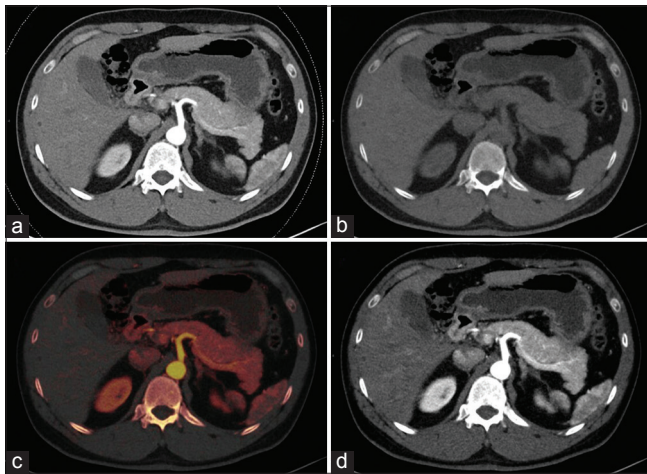

Figure 2: Various post-processing images from routine contrast-enhanced dual-energy computed tomography. (a) Axial blended image is derived from the blending of data from low- and high-energy images. (b) Virtual unenhanced image depicts the subtraction of contrast from the contrast-enhanced image. (c) In iodine overlay image, iodine-containing voxels are colour coded, usually in orange. (d) Virtual monochromatic low-energy image demonstrates increased contrast resolution with a better depiction of vascular structures.

Figure 3: This graph shows the attenuation of various materials (y-axis) and their changes with differing energy levels (X-axis). The insert image demonstrates the location of the various regions of interest for various body constituents. Calcium (white curve) and iodine (yellow curve) show increased attenuation at low energy levels. Muscle (orange curve) and bile (green curve) do not show a significant difference in attenuation with differing energy levels. Fat (purple curve) shows reduced attenuation as the energy level decreases.

to the atomic number of the material. Compton scattering is dominant at high energy levels and affects substances with low atomic numbers.[2,3] In low atomic number materials, such as soft tissue and muscle, there is only minimal difference in attenuation values with variation in energy levels. Conversely, in high atomic number materials, such as iodine and calcium, the attenuation value increases with a reduction in energy level.[3] By making use of this principle of comparing the attenuation of different materials when exposed to high and low energy levels, dual-energy CT can help to improve material differentiation.[4]
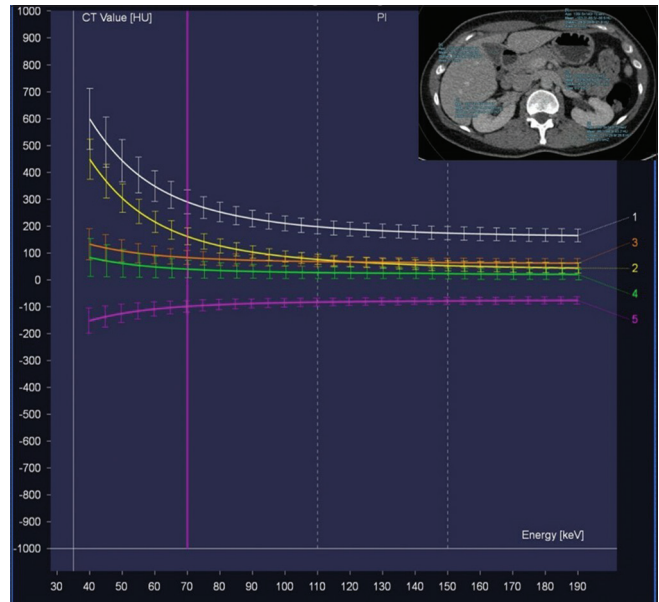
TYPES OF DUAL-ENERGY CT

The commonly used principles of dual-energy CT systems are:

Dual-source dual-energy CT

In this method, the two different tubes (sources) operating at two different voltage settings (high kVp and low kVp)
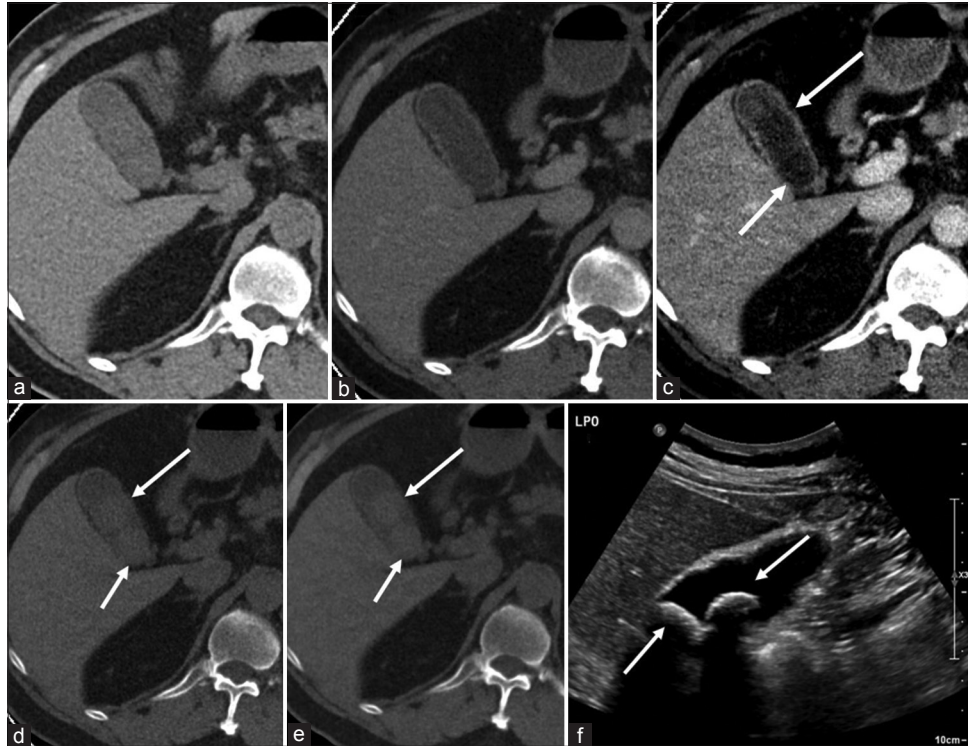
Figure 4: A 68-year-old male presented with non-specific abdominal pain. (a and b) Axial unenhanced and portal venous phase of the upper abdomen demonstrates no calcified gallstone. (c) Axial virtual monoenergetic image at low-energy (40 keV) demonstrates two large non-calcified gallstones (arrows), which are hypoattenuating compared to bile. (d and e) On axial virtual monoenergetic image at high-energy (190 keV) and virtual unenhanced image the gallstones are hyperattenuating (arrows) compared to bile. These were not appreciable on routine CT images. (f) Ultrasound confirms two large gallstones (arrows).
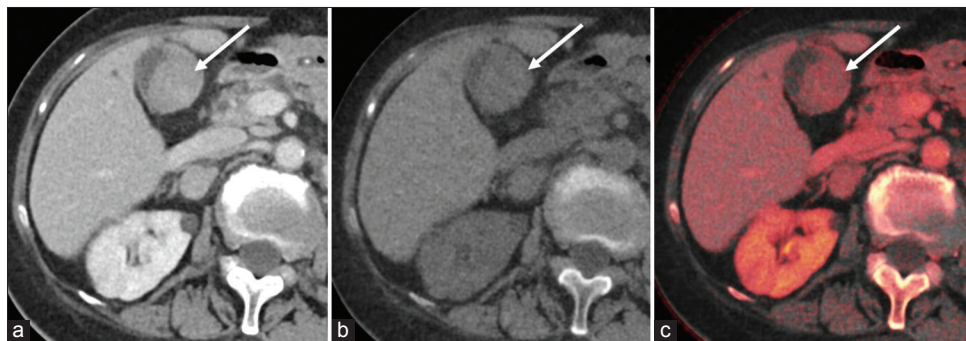

Figure 5: A 74-year-old female, known case of ovarian malignancy, computed tomography (CT) performed for staging. (a) Axial CT in the portal venous phase demonstrates a soft-tissue density lesion in the gallbladder (arrow) which was indeterminate for a solid lesion versus a non-calcified gallstone. (b) The axial virtual unenhanced image demonstrates a large soft tissue density lesion (arrow). (c) The axial iodine overlay map demonstrates iodine uptake within the lesion (arrow), confirming a solid lesion. The lesion was proven to be carcinoma of the gallbladder after surgery.

enable the acquisition of datasets with two different energy levels. There are also two sets of corresponding detectors, which are mounted in the gantry orthogonally oriented to the tubes.

Fast voltage switching

This principle utilizes a single source CT which is capable of rapid voltage switching (commonly between 80 and 140 kVp)
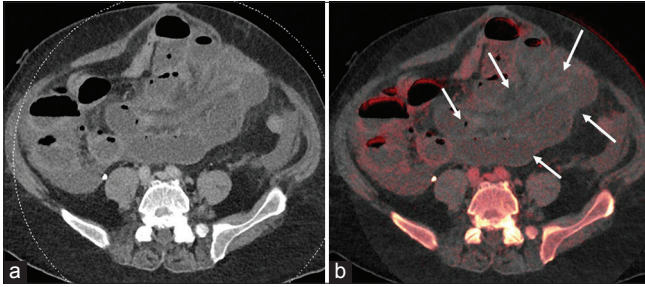
Figure 6: A 73-year-old male clinically presented with intestinal obstruction. (a) Axial contrast-enhanced computed tomography demonstrates multiple dilated small bowel loops secondary to adhesions, causing intestinal obstruction. (b) The axial iodine overlay map demonstrates reduced mural enhancement of the small bowel loops on the left side (arrows), consistent with bowel ischemia, which was not readily apparent in the routine images. The patient also had a prior right hemicolectomy with a stoma in the right upper abdomen (not shown).
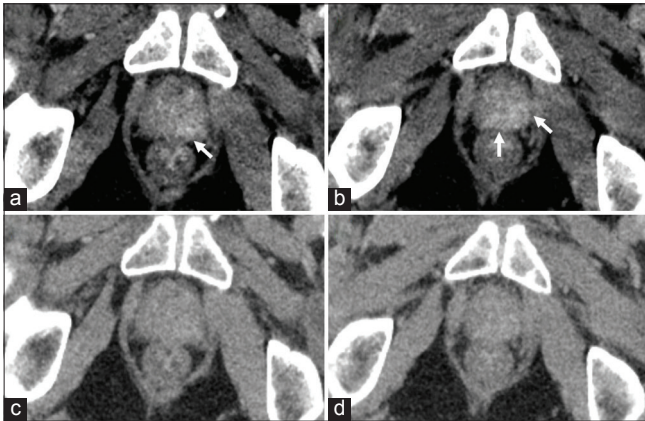

Figure 7: A 72-year-old male presented with non-specific loss of weight. (a and b) Axial virtual monoenergetic images at low-energy (50 keV) demonstrate asymmetric enhancement in the left peripheral zone in the posterolateral aspect. (c and d) The lesions were not apparent in the routine axial images. The patient was later investigated to have elevated prostate-specific antigen levels, and prostatic carcinoma was detected on histopathology.

to obtain two different datasets. These CTs are equipped with a single-layer detector.

Detector-based spectral imaging

This technique uses a single source CT with fixed voltage coupled with a dual-layered detector, which consists of a thin inner layer to absorb the low-energy photons and a thick outer layer to absorb the high-energy photons [Figure 1].[5-7]

DUAL-ENERGY CT ANALYSIS

For routine diagnostic interpretation, non-material-specific images can be generated by blending data from high- and low-energy images (1). The other commonly used post-processed images are:

Virtual unenhanced images

The acquired final image minus all contrast-enhanced structures results in the virtual unenhanced images.[5] Virtual unenhanced images may substitute a pre-contrast scan in some situations and reduce radiation exposure. However, the difference in attenuation values may vary up to 15 HU in virtual unenhanced compared with true unenhanced images.[5,6] Furthermore, the suppression of iodine may not be complete in all situations.[2]

Iodine-enhanced images

Contrast-enhanced dual-energy CT images minus water create iodine-enhanced images.[2] For better visualization, the iodine concentration may be superimposed on the grayscale anatomic image as a color map.[1] The enhancement can also be assessed quantitatively by measuring the amount of iodine in a specific region of interest (ROI).[4,7]

Virtual monoenergetic images

In low-energy images, the increased attenuation of materials with a high atomic number, like iodine and calcium, helps to enhance the contrast-to-noise ratio [Figure 2]. In high-energy images, beam hardening artifacts are reduced and can be used to reduce artifacts from metal hardware.[4,5]

Spectral HU curve

Spectral HU curves can be obtained using virtual monochromatic images by placing an ROI on the tissue and measuring the average CT number of the tissue at each monochromatic energy (from low to high keV). At lower energies, the attenuation of bone and high atomic number materials, like iodine and calcium, increases, whereas it decreases for fat. For water, the attenuation is zero at all energies.[2] The difference in attenuation of soft-tissue structures, like muscles and organs, at various energy levels is minimal [Figure 3].[4]

CLINICAL APPLICATIONS

Gallbladder

Non-calcified cholesterol containing gallstones are isoattenuating with bile on conventional CT images. Since the energy dependent X-ray attenuation curve is different for bile and fat, these cholesterol containing gallstones appear hypoattenuating to bile on low-keV images and hyperattenuating to bile on high-keV images. These stones are appreciated as hyperattenuating foci on virtual
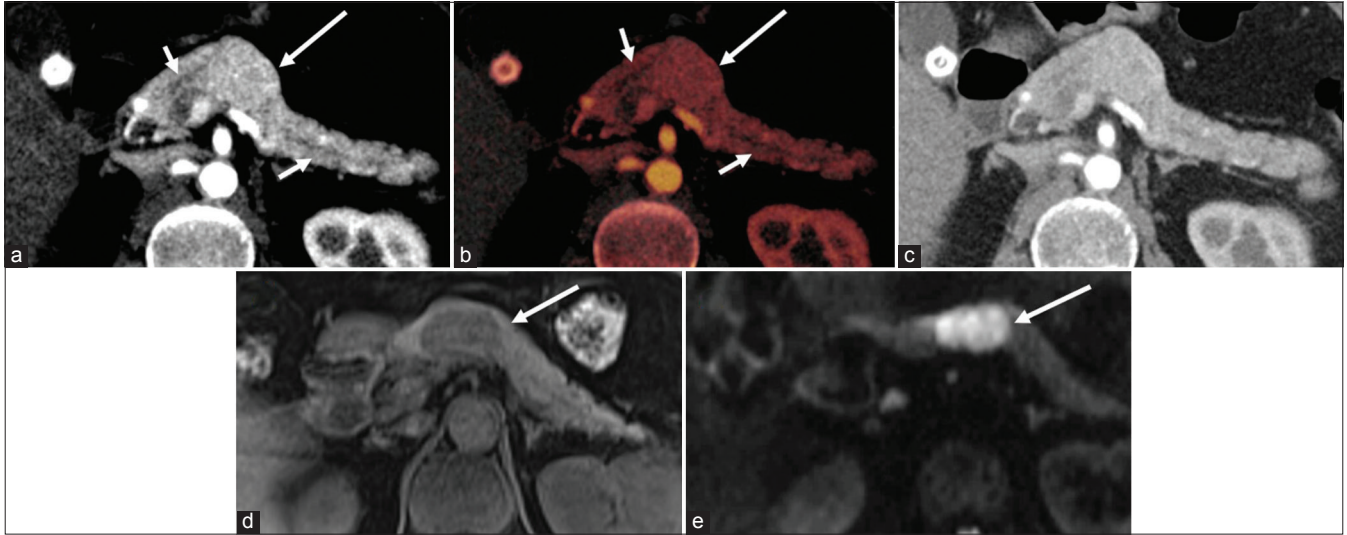
Figure 8: A 55-year-old male was referred for upper abdominal pain. (a and b) Axial virtual monoenergetic image at low-energy (50 keV) and Iodine overlay images demonstrate an ill-defined enhancing mass in the neck of the pancreas (long arrow in a and b). The non-dilated main pancreatic duct (small arrows in a and b) is also better demonstrated and obscuration of the main pancreatic duct can be seen at the level of mass. (c) On the routine axial computed tomography of the abdomen in the arterial phase, the mass was inconspicuous. (d and e) Axial magnetic resonance imaging confirmed the suspicious mass in the neck of the pancreas, which was hypointense on the T1-weighted fat-suppressed images (arrow in d) and demonstrated diffusion restriction, appearing bright on diffusion-weighted images (arrow in e) and dark on apparent diffusion coefficient (ADC) maps (not shown). The lesion was proven to be a well-differentiated neuroendocrine tumor in histopathology.
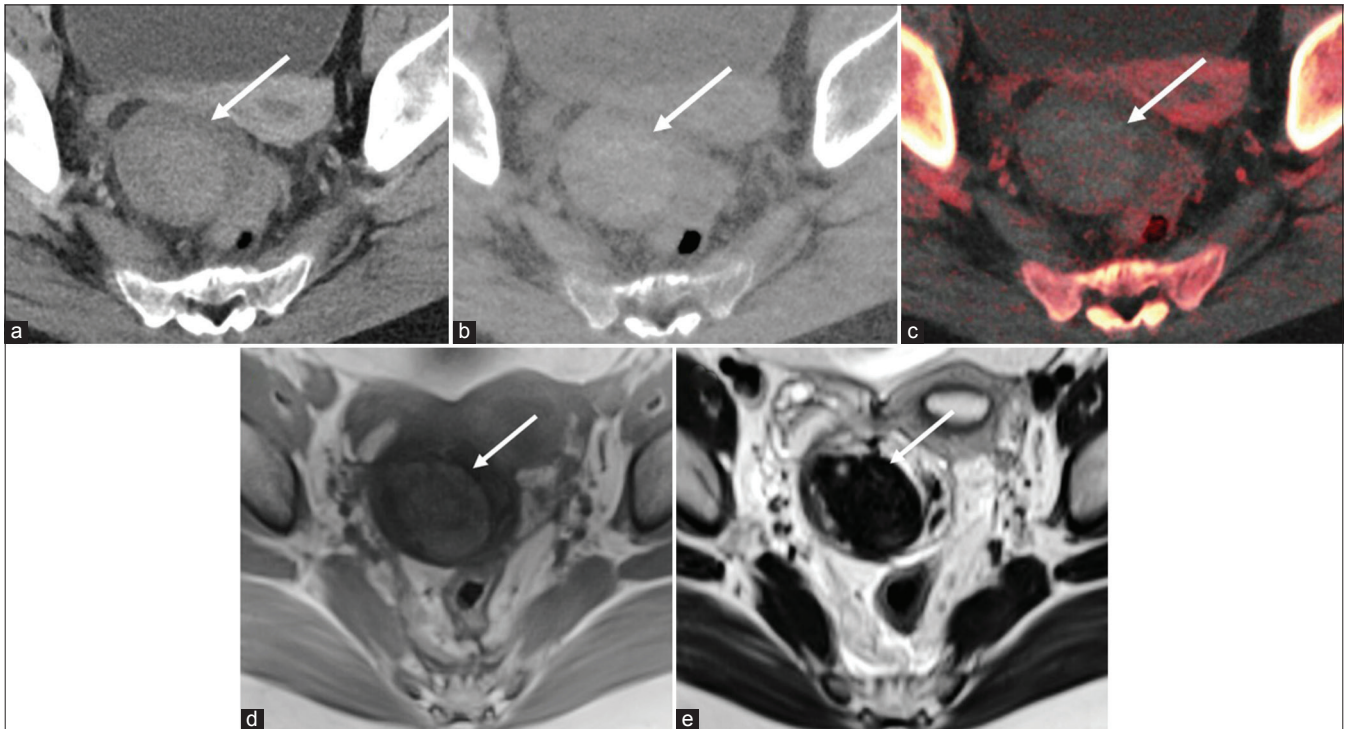

Figure 9: A 26-year-old female presented with lower abdominal pain. (a) Axial computed tomography of the pelvis in the portal venous phase demonstrates a circumscribed hyperdense lesion (arrow) closely abutting the posterior wall of the uterus (b) On the axial virtual unenhanced image, the lesion was hyperdense (arrow). (c) The lesion showed no iodine uptake on the axial iodine overlay map (arrow). These findings were consistent with a haemorrhagic lesion. (d and e) On the magnetic resonance imaging, the lesion was hyperintense on the axial T1-weighted image (arrow in d) and hypointense on the T2-weighted image (arrow in e). The imaging features were consistent with hemorrhage into a sub-serosal uterine fibroid.
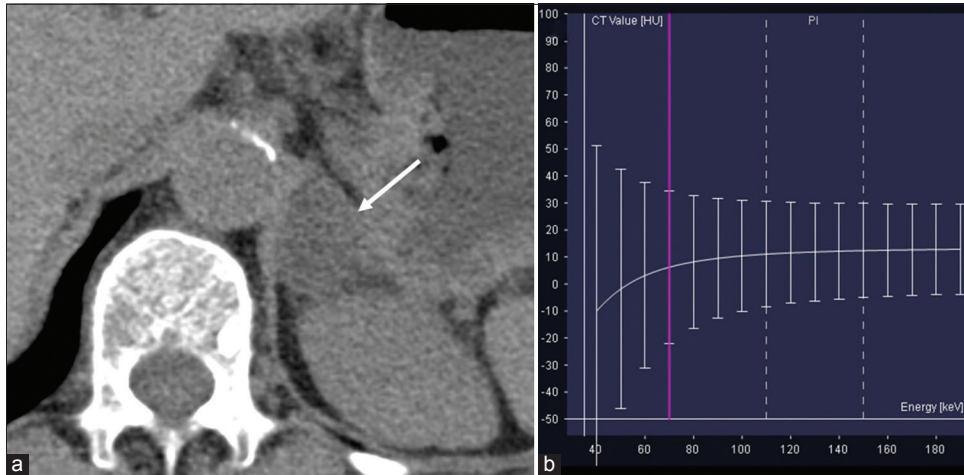
Figure 10: A 79-year-old male presented with the left adrenal incidentaloma. (a) Axial unenhanced computed tomography demonstrates a circumscribed hypodense left adrenal nodule (arrow). The unenhanced attenuation was + 12 hounsfield units within the nodule. (b) The spectral curve within the lesion is suggestive of fat content within, which is consistent with adenoma.
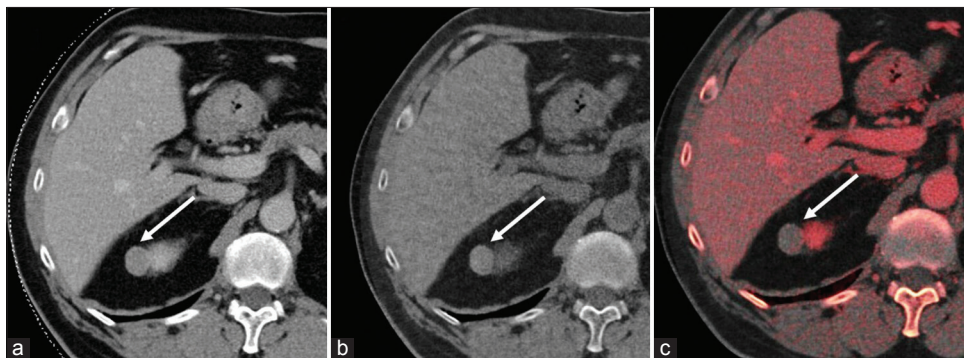

Figure 11: A 63-year-old male with non-specific abdominal pain. (a) Axial computed tomography of the abdomen in the portal venous phase demonstrates an incidental circumscribed hyperattenuating (+68 hounsfield units) lesion in the upper pole of the right kidney (arrow). The lesion was indeterminate for a solid enhancing lesion versus a hyperdense cyst. (b) The lesion was also hyperattenuating (+ 65 hounsfield units) on the axial virtual unenhanced image (arrow). (c) There was absence of iodine uptake on the axial iodine overlay map (arrow). The imaging features were suggestive of hyperdense cyst, and the possibility of an enhancing solid lesion was ruled out.

unenhanced images. The reason for the increased attenuation of cholesterol stones on virtual unenhanced images is attributed to increased high keV information on the dual-energy post-processing technique [Figures 4 and 5].[8-10]

Bowel

The use of low-keV virtual monoenergetic imaging improves the accuracy of detecting bowel ischemia in the setting of obstruction and vascular occlusion by increasing the difference in attenuation of ischemic and non-ischemic segments. The iodine overlay map depicts the absence of mural iodine uptake in the bowel that helps

to confirm ischemia [Figure 6].[11] Active hemorrhage and hyperenhancement of the bowel wall in inflammation are also well demonstrated on low-keV virtual monoenergetic images.[4,12]

Oncology

Monochromatic low-keV images and iodine maps also increase the contrast between the tumor and the adjacent normal parenchyma, improving lesion detection, the relationship of the tumor with adjacent structures, and distant metastases [Figures 7 and 8].[3,13-15]

Figure 12: A 67-year-old male, a known case of autosomal dominant polycystic kidney disease (ADPKD), presented with hematuria. (a) Axial computed tomography of the abdomen in the portal venous phase demonstrates diffusely enlarged kidneys with multiple cysts of varying sizes replacing the entire renal parenchyma consistent with the known ADPKD. No suspicious enhancing lesion is apparent. (b) However, a focal enhancing lesion was readily identified on the axial iodine overlay map (arrow). (c) The lesion was isodense on the axial virtual unenhanced image (arrow), confirming contrast uptake on iodine overlay map. The imaging features were suspicious for renal cell carcinoma, which was confirmed on histopathology
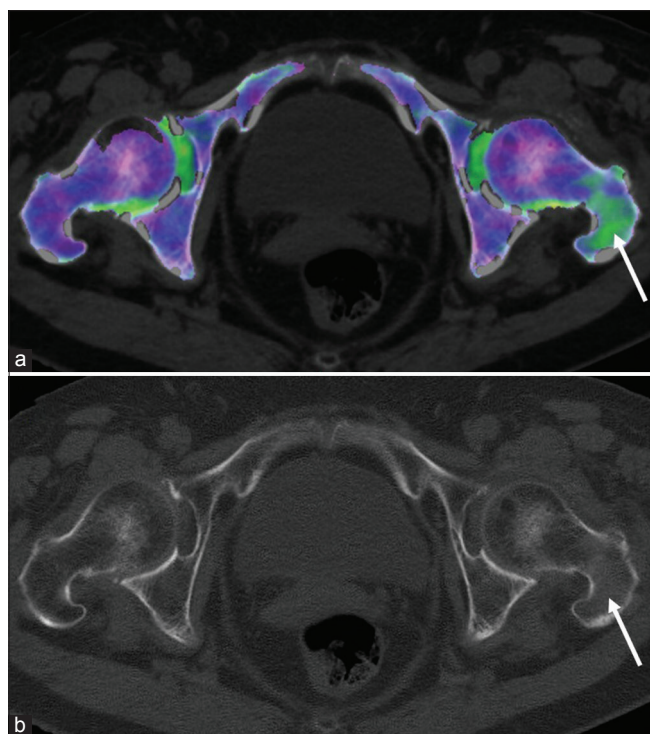

Figure 13: An 81-year-old female presented with persistent left hip pain. (a) The color-coded map demonstrates bone marrow edema (coded in green) in the left femur extending from the lesser trochanter to the greater trochanter along the posterior aspect (arrow). (b) There was corresponding faint sclerosis (arrow) on the axial bone window, which was not readily apparent without the aid of colour-coded maps. This was consistent with an undisplaced intertrochanteric fracture of the femur.

Hemorrhage

Virtual unenhanced images can confirm blood within the abdominopelvic cavity due to its hyperattenuating nature.

This may be beneficial in cases of acute intraabdominal hemorrhage or hemorrhagic lesions [Figure 9].[4]

Adrenal

Lipid-rich adenomas show lower attenuation at low keV due to the presence of fat, demonstrating higher specificity and sensitivity for the presence of intracellular lipids in some studies [Figure 10].[16,17]

Renal

Dual-energy CT provides a better evaluation of the unenhanced attenuation of renal lesions. This helps in the diagnosis of incidentally detected renal lesions, such as hyperdense cysts [Figure 11].[18,19] In patients with polycystic kidney disease, dual-energy CT expedites the unearthing of malignancy with increased diagnostic reliability [Figure 12].[20]

Bone

Dual-energy CT-generated edema images are used in detecting early bone fractures. Water density images demonstrating bone marrow edema can be generated by suppressing the calcium signal from the bone [Figure 13].[21]

Limitations

Lipiodol, made up of iodine combined with ethyl esters of fatty acids of poppyseed oil, is used in chemoembolization of hepatocellular carcinoma. The lipiodol uptake in hepatocellular carcinoma appears hyperdense on true non-contrast images; however, it is suppressed on virtual unenhanced images and appears iso to hypodense
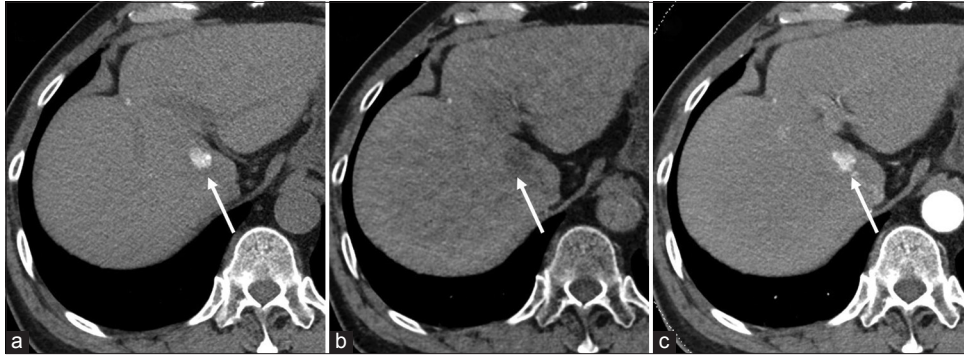
Figure 14: A 71-year-old male with a history of hepatocellular carcinoma post-chemoembolization. (a) Axial true unenhanced computed tomography (CT) demonstrates focal hyperdensity in the caudate lobe of the liver (arrow), due to lipiodol uptake within the hepatocellular carcinoma. (b) On the axial virtual unenhanced image, the lipiodol appears hypodense (arrow) due to the presence of iodine in lipiodol. (c) The arterial phase demonstrates focal hyperdensity (arrow), due to the lipiodol uptake and not due to arterial enhancement. If the true unenhanced image was unavailable in this study, there is a possibility of misinterpretation of hyperdensity in the arterial phase to be an arterial enhancement. This potential pitfall of suppression of lipiodol on the virtual unenhanced image must be remembered to avoid misinterpretation. Hence, we recommend obtaining true unenhanced CT in all cases of post-chemoembolization imaging of the liver.

Figure 15: A 52-year-old male presented with hematuria. (a) The axial contrast-enhanced image demonstrates a tiny calculus in the left kidney (arrow). (b) However, the calculus was not visible on the axial virtual unenhanced image.

which is attributed to the presence of iodine in lipiodol [Figure 14].[22,23]

Virtual unenhanced images are not sensitive for the detection of renal calculi <3 mm because calcification tends to be smaller [Figure 15]. [14]

CONCLUSION

Dual-energy CT of the abdomen provides ample added information to radiologists as compared to single-energy CT. Radiologists' awareness of the potential applications of dual-energy CT is essential to minimize the read time of the increased volume of post-processed images in routine practice. Limitations of the post-processed images must also be kept in mind to avoid misinterpretation.

Declaration of patient consent

Patient's consent not required as patient's identity is not disclosed or compromised.

Financial support and sponsorship

Nil.

Conflicts of interest

There are no conflicts of interest.

REFERENCES

1. Marin D, Boll DT, Mileto A, Nelson RC. State of the art: Dual-energy CT of the abdomen. Radiology 2014;271:327-42.
2. Tatsugami F, Higaki T, Nakamura Y, Honda Y, Awai K. Dual-

energy CT: Minimal essentials for radiologists. Jpn J Radiol 2022;40:547-59.

3. Agrawal MD, Pinho DF, Kulkarni NM, Hahn PF, Guimaraes AR, Sahani DV. Oncologic applications of dual-energy CT in the abdomen. Radiographics 2014;34:589-612.

4. Murray N, Darras KE, Walstra FE, Mohammed MF, McLaughlin PD, Nicolaou S. Dual-energy CT in evaluation of the acute abdomen. Radiographics 2019;39:264-86.

5. Adam SZ, Rabinowich A, Kessner R, Blachar A. Spectral CT of the abdomen: Where are we now? Insights Imaging 2021;12:138.

6. Goo HW, Goo JM. Dual-energy CT: New horizon in medical imaging. Korean J Radiol 2017;18:555-69.

7. Hokamp NG, Maintz D, Shapira N, Chang DH, Noël PB. Technical background of a novel detector-based approach to dual-energy computed tomography. Diagn Interv Radiol 2020;26:68-71.

8. Ratanaprasatporn L, Uyeda JW, Wortman JR, Richardson I, Sodickson AD. Multimodality imaging, including dual-energy CT, in the evaluation of gallbladder disease. Radiographics 2018;38:75-89.

9. Lee HA, Lee YH, Yoon KH, Bang DH, Park DE. Comparison of virtual unenhanced images derived from dual-energy CT with true unenhanced images in evaluation of gallstone disease. AJR Am J Roentgenol 2016;206:74-80.

10. Silva AC, Morse BG, Hara AK, Paden RG, Hongo N, Pavlicek W. Dual-energy (spectral) CT: Applications in abdominal imaging. Radiographics 2011;31:1031-46.

11. Darras KE, McLaughlin PD, Kang H, Black B, Walshe T, Chang SD, *et al.* Virtual monoenergetic reconstruction of contrast-enhanced dual energy CT at 70keV maximizes mural enhancement in acute small bowel obstruction. Eur J Radiol 2016;85:950-6.

12. Sun H, Hou XY, Xue HD, Li XG, Jin ZY, Qian JM, *et al.* Dual-source dual-energy CT angiography with virtual unenhanced images and iodine map for active gastrointestinal bleeding: Image quality, radiation dose and diagnostic performance. Eur J Radiol 2015;84:884-91.

13. Karçaaltıncaba M, Aktaş A. Dual-energy CT revisited with multidetector CT: Review of principles and clinical applications. Diagn Interv Radiol 2011;17:181-94.

14. Heye T, Nelson RC, Ho LM, Marin D, Boll DT. Dual-energy CT applications in the abdomen. AJR Am J Roentgenol 2012;199:S64-70.

15. Prokesch RW, Chow LC, Beaulieu CF, Bammer R, Jeffrey RB Jr. Isoattenuating pancreatic adenocarcinoma at multi-detector row CT: Secondary signs. Radiology 2002;224:764-8.

16. Lestra T, Mulé S, Millet I, Carsin-Vu A, Taourel P, Hoeffel C. Applications of dual energy computed tomography in abdominal imaging. Diagn Interv Imaging 2016;97:593-603.

17. Glazer DI, Maturen KE, Kaza RK, Francis IR, Keshavarzi NR, Parker RA, *et al.* Adrenal incidentaloma triage with single-source (fast-kilovoltage switch) dual-energy CT. AJR Am J Roentgenol 2014;203:329-35.

18. Neville AM, Gupta RT, Miller CM, Merkle EM, Paulson EK, Boll DT. Detection of renal lesion enhancement with dual-energy multidetector CT. Radiology 2011;259:173-83.

19. Ascenti G, Mazziotti S, Mileto A, Racchiusa S, Donato R, Settineri N, *et al.* Dual-source dual-energy CT evaluation of complex cystic renal masses. AJR Am J Roentgenol 2012;199:1026-34.

20. Glomski SA, Wortman JR, Uyeda JW, Sodickson AD. Dual energy CT for evaluation of polycystic kidneys: A multi reader study of interpretation time and diagnostic confidence. Abdom Radiol (NY) 2018;43:3418-24.

21. Akisato K, Nishihara R, Okazaki H, Masuda T, Hironobe A, Ishizaki H, *et al.* Dual-energy CT of material decomposition analysis for detection with bone marrow edema in patients with vertebral compression fractures. Acad Radiol 2020;27:227-32.

22. Lipiodol [Package Insert]. Princeton, NJ: Guerbet LLC; 2020.

23. Flemming BP, De Cecco CN, Hardie AD. Limitation of virtual noncontrasted images in evaluation of a liver lesion status post transarterial chemoembolization. J Comput Assist Tomogr 2016;40:557-9.